ADVANCED ENERGY MATERIALS
www.advenergymat.de

Unveiling Chemically Robust Bimetallic Squarate-Based Metal–Organic Frameworks for Electrocatalytic Oxygen Evolution Reaction

*Sharath Kandambeth, Vinayak. S. Kale, Dong Fan, Jeremy A. Bau, Prashant M. Bhatt, Sheng Zhou, Aleksander Shkurenko, Magnus Rueping, Guillaume Maurin, Osama Shekhah, and Mohamed Eddaoudi**

Here, this work reports an innovative strategy for the synthesis of chemically robust metal–organic frameworks (MOFs), and applies them as catalysts for the electrocatalytic oxygen evolution reaction (OER). A bimetallic squarate-based MOF (Sq-MOF) with a zbr topology serves as an excellent platform for electrocatalytic OER owing to its open porous structure, high affinity toward water, and presence of catalytically active 1D metal hydroxide strips. By regulating the Ni^{2+} content in a bimetallic squarate MOF system, the electrochemical structural stability toward OER can be improved. The screening of various metal ratios demonstrates that Ni_3Fe_1 and Ni_2Fe_1 Sq-zbr-MOFs show the best performance for electrocatalytic OER in terms of catalytic activity and structural stability. Ni_2Fe_1 Sq-zbr-MOF shows a low overpotential of 230 mV (at 10 mA cm^{-2}) and a small Tafel slope of 37.7 mV dec^{-1}, with an excellent long-term electrochemical stability for the OER. Remarkably, these overpotential values of Ni_2Fe_1 Sq-zbr-MOF are comparable with those of the best-performing layered double hydroxide (LDH) systems and outperforms the commercially available noble-metal-based RuO_2 catalyst for OER under identical operational conditions.

1. Introduction

Global energy demand is increasing because of rapid population growth.[1] The extensive use of nonrenewable fossil fuels is considered to be responsible for ecological imbalances such as global warming and depletion of ozone layer.[2] Hydrogen is being considered as a future source of clean energy owing to its high energy density/heat value combined with its ecofriendly nature.[3] Electrochemical water splitting is considered as one of the most effective approaches for producing high-purity H_2 using energy from renewable sources.[4] This electrochemical process involves, two half-cell reactions, e.g. hydrogen evolution reaction (HER) and oxygen evolution reaction (OER), simultaneously occurring at the cathode and anode, respectively.[5] Compared with the HER, the OER mechanism is extremely complex and kinetically sluggish because it involves a multistep four-electron-transfer reaction ($4OH^- \rightarrow 2H_2O + O_2 + 4e^-$). This calls for an efficient OER catalyst to improve the overall energy efficiency of electrochemical water splitting.[6]

Presently, noble metal-based oxides such as RuO_2 and IrO_2 are the commonly used OER catalysts.[7] However, because of scarcity and high cost of noble metals, researchers are shifting their focus toward developing novel OER catalysts based on inexpensive transition metals encompassing optimized electrical conductivity and accessibility to active sites.[8] Previously, in alkaline electrolytes, mixed-metal (Ni–Fe) layered double hydroxides (LDHs) were the most promising cost-effective electrocatalysts for the OER reaction.[9] However, mechanistic studies demonstrated that catalytically active OER sites are only partially accessible

S. Kandambeth, V. S. Kale, P. M. Bhatt, S. Zhou, A. Shkurenko, O. Shekhah, M. Eddaoudi
Functional Materials Design
Discovery and Development Research Group (FMD3)
Advanced Membranes and Porous Materials (AMPM) Center
Physical Science and Engineering (PSE) Division
King Abdullah University of Science and Technology (KAUST)
Thuwal 23955-6900, Kingdom of Saudi Arabia
E-mail: mohamed.eddaoudi@kaust.edu.sa

D. Fan, G. Maurin
ICGM
Université Montpellier
CNRS
ENSCM
Montpellier 34095, France

J. A. Bau, M. Rueping
KAUST Catalysis Center
KCC
King Abdullah University of Science and Technology (KAUST)
Thuwal 23955-6900, Kingdom of Saudi Arabia

The ORCID identification number(s) for the author(s) of this article can be found under https://doi.org/10.1002/aenm.202202964.

DOI: 10.1002/aenm.202202964

to reactants in the excited state because of the low porosity of LDHs.[10] In this regard, metal–organic frameworks (MOFs) appear as promising candidates for OER because of their predesignable open porous structure, enhanced catalytic site exposure, and ease of functional tunability.[11] Therefore, this family of hybrid materials offers a unique opportunity to design a catalyst integrating desired OER catalytic sites and an adequate pore network for optimal reactant diffusion and accessibility to these catalytic sites.[11]

Nevertheless, very few studies have focused on pristine MOFs as OER electrocatalysts.[12] The two main reasons behind the limited electrocatalytic performance of this class of porous materials are generally their low electrical conductivity and poor electrochemical stability.[13] Indeed most of the reported MOF-based OER catalysts were obtained from in situ conversion/decomposition of MOFs on layered hydroxides under electrochemical reaction conditions.[13] To address these limitations, we developed a novel bimetallic squarate-based MOF (Sq-MOF) having ultrahigh electrochemical structural stability in alkaline (1.0 M KOH) electrolytes and an excellent OER activity owing to its one-dimensional (1D) strips/chains of bimetallic metal hydroxide chains. Compared with the conventional zero-dimensional metal carboxylate cluster linked 3D MOFs, these chains act as both electrocatalytically active sites, while they favor a more efficient charge transport.[12b,c] Furthermore, compared with mixed-metal LDHs, the open pore channels of this novel MOF enable a fast diffusion of electrolytes and enhanced exposure/availability of catalytically active sites to reactants.

We selected Co, Ni, and Fe ions as preliminary candidates for synthesizing bimetallic Sq-MOFs because of their abundance, low cost, and potentially high OER activity. After screening various bimetallic ratios for squarate-based MOFs, the Ni_2Fe_1 Sq-MOF with **zbr** topology (Ni_2Fe_1 Sq-**zbr**-MOF) was found to be the most efficient and robust OER catalyst in 1.0 M KOH; this material shows a low overpotential of 230 mV (at 10 mA cm^{-2}), a small Tafel slope of 37.7 mV dec^{-1}, and excellent long-term electrochemical stability for OER. Remarkably, under identical operational conditions, this bimetallic Ni_2Fe_1 Sq-**zbr**-MOF was demonstrated to outperform commercially available noble-metal-based RuO_2 OER catalyst.

2. Results and Discussion

2.1. Synthesis of Bimetallic Sq-MOFs (Electrocatalysts)

Bimetallic Sq-MOFs (Co-Ni, Ni-Fe, Co-Fe) were synthesized in a 100 mL Teflon-lined reactor under hydrothermal reaction conditions at 220 °C (details are in the Experimental Section) (**Figure 1**). After the reaction, these Sq-MOFs were purified using deionized (D. I.) water and acetone. The bimetallic Sq-MOFs were obtained as single crystals with varying colors depending on metal ratios: from magenta to green (Co-Ni, **Figure 2**a), from green to yellow (Fe-Ni, Figure 2b), and from red to magenta (Co-Fe, Figure 2c). Single crystal X-ray diffraction (SXRD) and powder X-ray diffraction (PXRD) analysis were used to determine the crystal structures of bimetallic metal Sq-MOFs. When squaric acid reacts with metal ions such as Co^{2+}, Ni^{2+}, and Fe^{2+}, MOFs are formed with either a **zbr** or a **nbo-b** topology (Figure 1). The MOF with **zbr** topology (Sq-**zbr**-MOF) possesses catalytically active 1D metal hydroxide chains/strips, making it a highly desirable candidate for electrochemical OER applications (Figure 1c, Figure S1, Supporting Information). Furthermore, the Sq-**zbr**-MOF contains rhombohedral-shaped 1D open pore

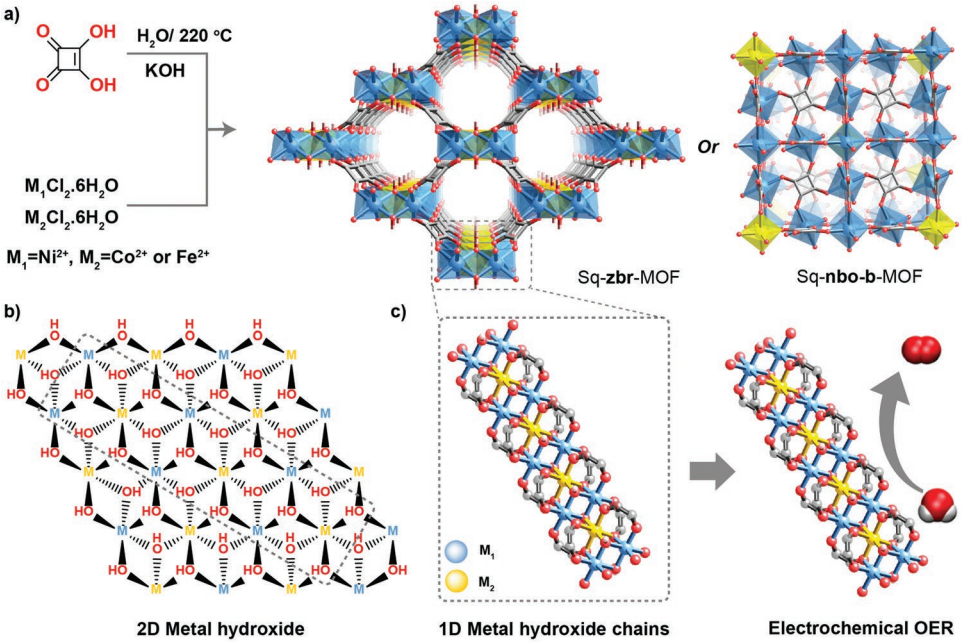

Figure 1. Synthesis of bimetallic Sq-MOFs. a) Scheme for the hydrothermal synthesis of bimetallic Sq-MOFs. b) Schematic of 1D-metal hydroxide stripe present in 2D metal hydroxide. c) Schematic of 1D-metal hydroxide stripe present in Sq-zbr-MOFs and schematic of the oxygen evolution reaction (OER) activity of 1D-metal hydroxide stripes present in the Sq-zbr-MOFs.

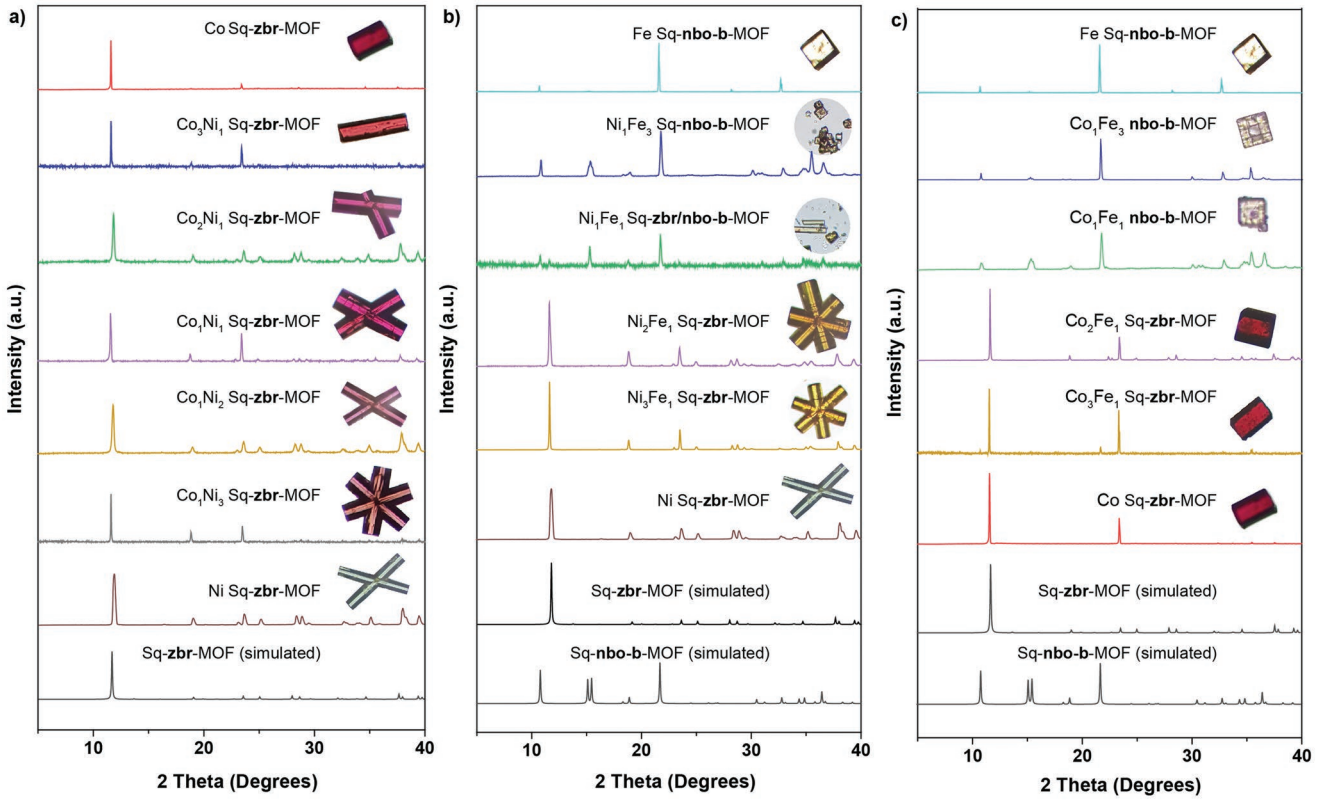

Figure 2. Powder X-ray diffraction (PXRD) of bimetallic Sq-MOFs. a) Co-Ni Sq-zbr-MOF, b) Fe-Ni Sq- zbr/nbo-b-MOF, and c) Fe-Co Sq zbr/nbo-b-MOF.

channels, which are accessible to water molecules for the OER reaction (Figure 1a). In the Sq-**zbr**-MOF, the 1D metal hydroxide chains comprise continuous $M_3(OH)_2$ strips where the hydroxyl (–OH) oxygen atoms are μ^3 bridged to metal ions (Figure 1b). The structural similarity of these 1D metal hydroxide chains in Sq-**zbr**-MOF to LDH strips (Figure 1) makes this new MOF highly attractive for the electrochemical OER reaction.

In contrast, the MOF with **nbo-b** topology (Sq-**nbo-b**-MOF) does not have open pore channels, it is unsuitable for OER (Figure 1a). This structure comprises isolated M(II) octahedral polyhedra, which are connected via squarate dianions. The M(II) ions are then coordinated to four squarate oxygens and two oxygen atoms of water molecules (Figure 1a). Unlike the Sq-**zbr**-MOF, the Sq-**nbo-b**-MOF lacks μ^3 bridged –OH groups and 1D-metal hydroxide strips. Therefore, compared to the Sq-**zbr**-MOF, the Sq-**nbo-b**-MOF is less desirable for the OER. Co^{2+} and Cu^{2+} metal ions have been previously shown to form the **zbr** topology, [14] whereas Ni^{2+} and Fe^{2+} have only been reported to form the **nbo-b** topology. [15] Our experiments demonstrated that the Ni Sq-**zbr**-MOF with **zbr** topology ($[Ni_3(C_4O_4)_2(OH)_2].2.68H_2O$) can be prepared in high yield for the first time by performing the hydrothermal reaction at high temperatures (between 220 °C to 250 °C). The **nbo-b** topology of Ni squarate MOF was isolated as the major phase at temperatures in between 150 °C to 200 °C. In contrast, our attempts to synthesize the **zbr** topology of Fe^{2+} were unsuccessful; only the **nbo-b** topology was obtained at all reaction temperatures, including those as high as 220 °C.

PXRD analysis evidenced that the Co–Ni bimetallic squarate MOFs form the desired **zbr** topology in all Co^{2+} and Ni^{2+} concentration variations (Figure 2a). However, the nature of these phases in Co-Fe and Ni-Fe bimetallic Sq-MOFs depends on the ratio of the concentration of bimetallic metal ions (Figure 2b,c). In the case of bimetallic Co–Fe and Ni–Fe, they exhibit the desired **zbr** structure at Fe^{2+} loading up to 33%. A mixed phase of **zbr** and **nbo-b** structures was obtained at 1:1 ratios of Ni–Fe. Only the undesired **nbo-b** topology was observed at >50% Fe^{2+} incorporation in the reaction mixture (Figure 2b). The SXRD analysis of Ni Sq-**zbr**-MOF ($[Ni_3(C_4O_4)_2(OH)_2].2.68H_2O$) and Ni_2Fe_1 Sq-**zbr**-MOF ($[Fe_1Ni_2(C_4O_4)_2(OH)_2]$ $2.71H_2O$) revealed that these Sq-**zbr**-MOFs crystallize in a monoclinic system with a space group *C2/m*. The rhombohedral-shaped pore channels of these Sq-**zbr**-MOFs contain water molecules. Because of the close electron density matching of Fe^{2+}, Co^{2+}, and Ni^{2+}, we were unable to localize the exact distribution of the bi-metallic ions in the 1D metal hydroxide strips (Section S4, Supporting Information).

Fourier transform infrared spectroscopy (FTIR) studies demonstrated the formation of metal squarate linkages in a bimetallic squarate system (Figures S2–S4, Supporting Information). When squarate carbonyl groups were complexed with metal ions, symmetric and asymmetric stretching bands (1800 and 1637 cm^{-1}) are shifted to lower wavenumbers (1537 cm^{-1}) (Figure S2a, Supporting Information). Furthermore, the presence of μ^3 bridged hydroxyl (–OH) functionality in the Sq-**zbr**-MOFs can be detected by the appearance of a distinct signal at ≈3600 cm^{-1} (Figure S2, Supporting Information). However, the

stretching band corresponding to μ^3–bridged hydroxyl (–OH) was absent in the FTIR spectra of Sq-**nbo-b** -MOFs; only a broad peak corresponding to adsorbed water molecules is observed (Figures S3 and S4, Supporting Information). Energy-dispersive X-ray spectroscopy (EDX) mapping was used to determine the ratio of bimetallic ions in these Sq-MOFs (Figures S5–S8, Supporting Information). The observed ratios of mixed metal ions were found to be proportional to the molar ratios of the starting metal ion precursor.

To examine the thermal stability of bimetallic squarate MOFs (Sq-MOF), thermogravimetric analysis (TGA) was performed under nitrogen flow. TGA analysis revealed that the thermal stability of bimetallic Co_1Ni_2 and Ni_2Fe_1 Sq-**zbr**-MOFs was almost similar to that of the pristine monometallic Sq-**zbr**-MOF (Co Sq-**zbr**-MOF, Ni Sq-**zbr**-MOF). These dehydrated bimetallic Sq-MOFs retain thermal stability of up to 300 °C after an initial loss of adsorbed water molecules from the pores (8–10 wt%) (Figure S9, Supporting Information).

To examine the permanent porosity of Sq-MOFs, water vapor adsorption experiments were performed at 25 °C. Monometallic Sq-MOFs (Co Sq-**zbr**-MOF, Ni Sq-**zbr**-MOF) and bimetallic Sq-MOF (Ni_2Fe_1 Sq-**zbr**-MOF) demonstrate type I reversible water vapor uptake. This highlights the high water affinity of these MOFs which could be beneficial for improving mass transport properties of reactants at high current density during electrocatalytic water splitting. The total water vapor uptake of Sq-**zbr**-MOFs was estimated to be ≈10 wt% (Figure S10, Supporting Information). However, Fe Sq-**nbo-b**-MOF with a **nbo-b** topology does not show significant water vapor uptake because of its nonporous structure (Figure S10d, Supporting Information). Multiple attempts to evaluate the surface area of Sq-**zbr**-MOF from N_2 adsorption were not successful because of their smaller pore aperture (4.1 × 4.3 Å) compared with the kinetic diameter of N_2.[16]

The chemical stability of bimetallic Sq-MOFs was investigated by treating the samples in 1.0 M KOH for 3 days. These Sq-MOFs were washed with water, acetone after KOH treatment, and then their PXRD was measured. Monometallic and bimetallic Sq-MOFs demonstrate high chemical stability in basic conditions (1.0 M KOH) as revealed by their PXRD patterns, which remained unchanged after this long-term treatment (Figure S11, Supporting Information). The high chemical stability of Sq-MOFs under basic conditions makes them attractive candidates for electrochemical OER. Moreover, the crystal field stabilization energy of metal ions and squarate oxygen atoms in Sq-MOFs is higher than that of metal ions and water;

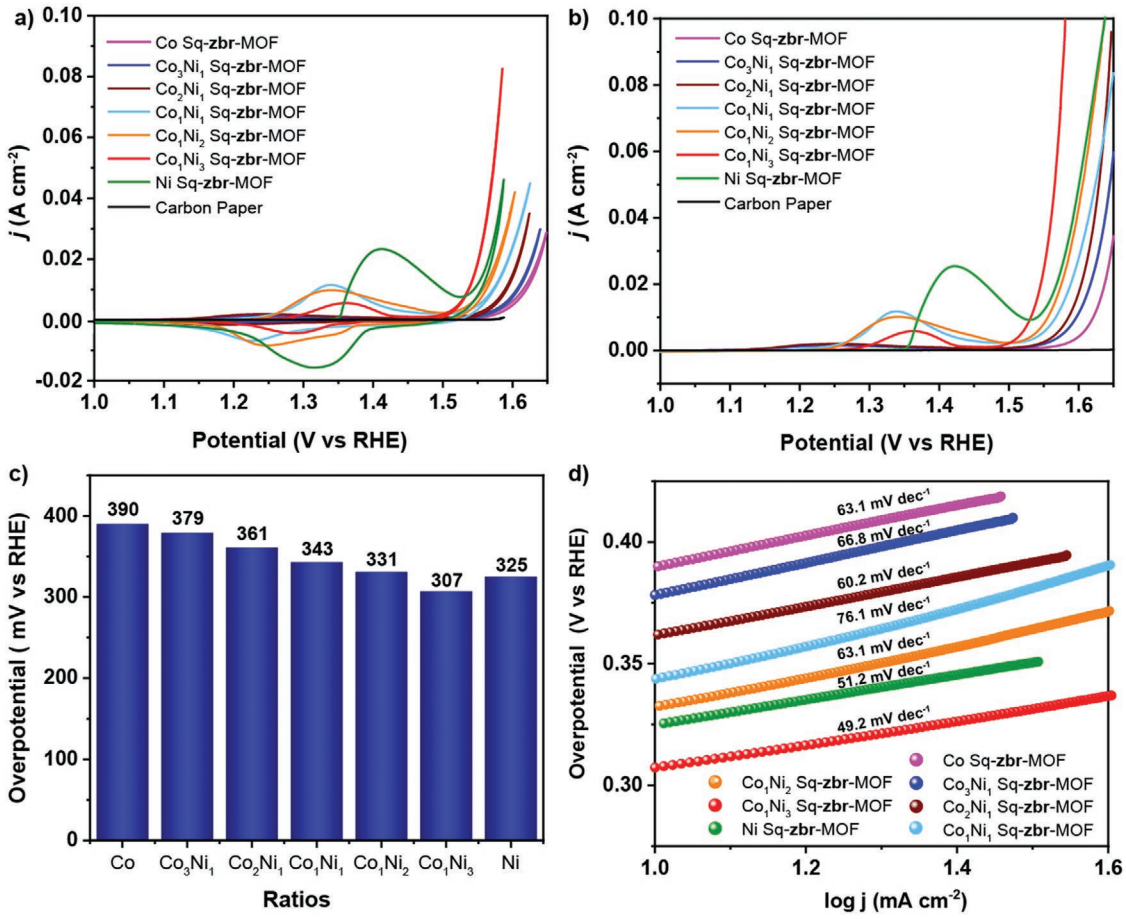

Figure 3. Electrochemical oxygen evolution activity of Co-Ni Sq-zbr-MOFs. a) Cyclic voltammetry (CV) and b) linear sweep voltammetry (LSV) of Co-Ni Sq-zbr-MOFs at a scan rate of 5 mVs^{-1}. c) Comparison of overpotential values of Co-Ni Sq-zbr-MOFs at 10 mA cm^{-2}. d) Tafel slopes of Co-Ni Sq-zbr-MOFs.

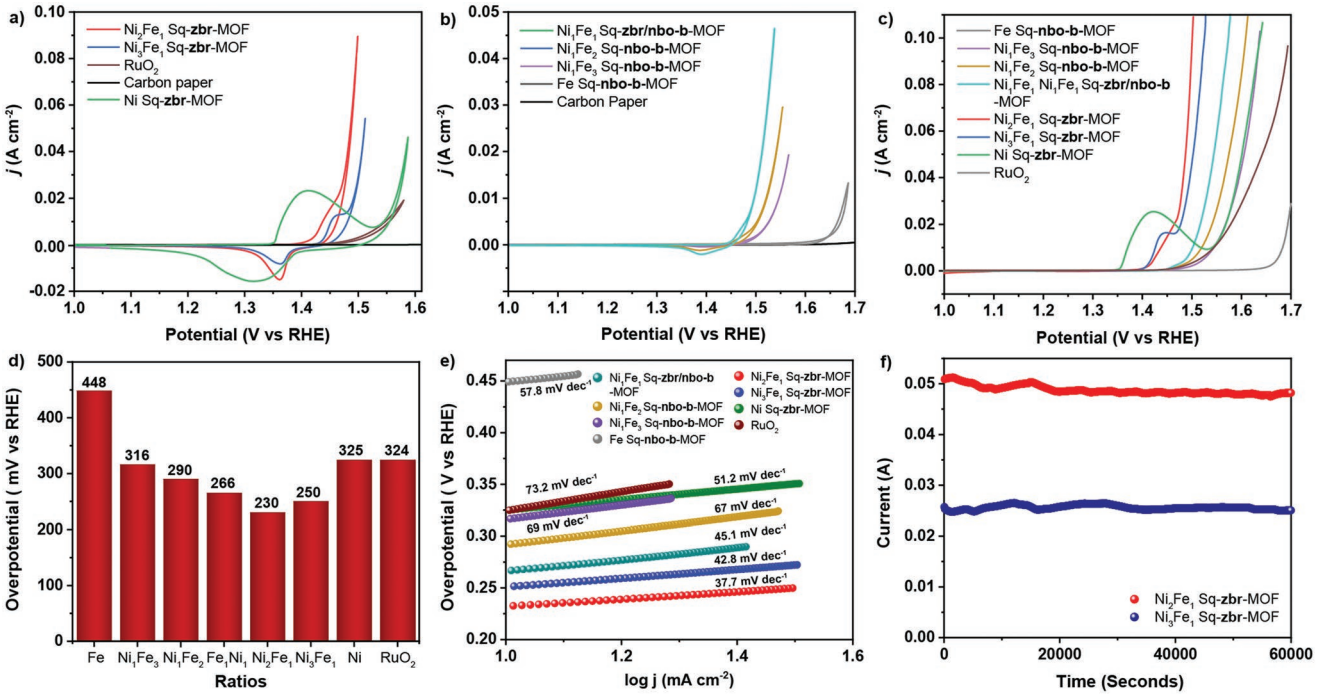

Figure 4. Electrochemical oxygen evolution activity of Fe-Ni Sq-zbr-MOFs. a) Cyclic voltammetry (CV) of Fe-Ni Sq- zbr-MOFs compared with commercial RuO_2 at a scan rate of 5 mVs^{-1}. b) CV of Fe-Ni nbo-b- Sq-MOFs at a scan rate of 5 mVs^{-1}. c) Linear sweep voltammetry (LSV) of Fe-Ni Sq-MOFs at a scan rate of 5 mVs^{-1}. d) Comparison of overpotential values of Fe-Ni Sq-MOFs at a current density of 10 $mAcm^{-2}$. e) Tafel slopes of Ni-Fe Sq-MOFs. f) Prolonged chronoamperometric profiles Ni_2Fe_1 Sq-zbr-MOF and Ni_3Fe_1 Sq-zbr-MOF show high catalytic stability.

this is the main reason for MOFs high hydrolytic structural stability. [16]

2.2. Electrochemical Performance

OER activity of bimetallic Sq-MOFs was evaluated in three electrode configurations using alkaline 1.0 M potassium hydroxide (KOH) as an electrolyte, mercury-mercuric oxide (Hg/HgO) as a reference electrode, and platinum wire (Pt) as a counter electrode (**Figures 3** and 4). Drop casting was used to prepare the electrode from the active catalyst material on carbon paper support (details in Experimental Section). We evaluated the OER performance of blank carbon paper support, which demonstrates negligible OER activity compared to the active bimetallic Sq-MOF catalyst (Figure 3a,b). The overpotential of bimetallic Sq-MOF catalysts was assessed using cyclic voltammetry (CV) and linear sweep voltammetry (LSV) measurements at a scan rate of 5 mVs^{-1}. CV measurements of Co–Ni bimetallic Sq-**zbr**-MOF show a redox couple of >1.25 V (versus RHE) (scan rate, 5 mVs^{-1}), which corresponds to a redox M^{2+}/M^{3+} reaction (Figure 3a). Note that by increasing Ni^{2+} content in the bimetallic Sq-**zbr**-MOF, the redox peak current density gradually enhanced and shifted to a higher potential (Figure 3a). To avoid the redox capacitive current contribution, overpotential was calculated from the CV discharge curves (Figure 3a). At a current density of 10 mA cm^{-2}, the overpotentials of monometallic Co and Ni Sq-**zbr**-MOFs were 390 and 325 mV, respectively (Figure 3c). Compared with monometallic Sq-**zbr**-MOFs, bimetallic Co-Ni Sq-**zbr**-MOF demonstrated a lower overpotential. The Co_1Ni_3 Sq-**zbr**-MOF is the most efficient OER catalyst because it shows a lower overpotential of 307 mV at a current density of 10 mA cm^{-2} (Figure 3c). The Tafel slope analysis of bimetallic Co_1Ni_3 Sq-**zbr**-MOF demonstrates a lower value of 49.2 mV dec^{-1} compared to the monometallic Co Sq-**zbr**-MOF (63.1 mV dec^{-1}) and Ni Sq-**zbr**-MOF (51.2 mV dec^{-1}) (Figure 3d). This result shows that Co_1Ni_3 Sq-**zbr**-MOF has faster OER reaction kinetics compared to monometallic Sq-**zbr**-MOF, which explains its lower overpotential. The Tafel slope values of Co_1Ni_3 Sq-**zbr**-MOF show that OER reaction kinetics involved the $4e^-$ transfer process, which is similar to LDH systems. A prolonged chronoamperometric test at a constant overpotential of 340 mV was performed to evaluate the electrochemical stability of Co_1Ni_3 Sq-**zbr**-MOF. After 15 h of the chronoamperometric test, ≈90% of current density was retained (Figure S12, Supporting Information). After the chronoamperometric test, the PXRD of the Co_1Ni_3 Sq-**zbr**-MOF electrode revealed the retention of characteristic Bragg peaks, demonstrating the high electrochemical structural stability of Co_1Ni_3 Sq-**zbr**-MOFs (Figure S12, Supporting Information).

We further examined the overpotential of Ni-Fe bimetallic Sq-MOF (Figure 4). Upon incorporating Fe^{2+} in the Ni Sq-**zbr**-MOF system, we observed a significant decrease in the overpotential values (Figure 4d). At a current density of 10 mA cm^{-2}, Ni_3Fe_1 and Ni_2Fe_1 Sq-**zbr**-MOFs demonstrated low overpotential values of 250 and 230 mV, respectively (Figure 4d). The lower overpotential values for Ni_3Fe_1 and Ni_2Fe_1 Sq-**zbr**-MOFs reveal their high catalytic activity for electrochemical OER. The above mentioned overpotential values are comparable to the best performing LDH systems.[17] Furthermore, Ni_3Fe_1 and Ni_2Fe_1

Sq-**zbr**-MOFs show a low Tafel slope of 42.8 and 37.7 mV dec^{-1}, respectively, indicating fast kinetics toward the OER reaction (Figure 4e). The high affinity of bimetallic Sq-**zbr**-MOFs for water molecules as shown by the water adsorption isotherm (Figure S10, Supporting Information) could be a reason for the low Tafel slope values. The Ni_2Fe_1 Sq-**zbr**-MOF shows low overpotential at higher current density because of its low Tafel slope and open porous structure to water molecules. LSV analysis demonstrated that Ni_2Fe_1 Sq-**zbr**-MOF could achieve an overpotential of 243 and 260 mV at a current density of 20 and 50 mA cm^{-2}, respectively (Figure 4b). Under identical experimental conditions, the overpotential values of bimetallic Ni_3Fe_1 and Ni_2Fe_1 Sq-**zbr**-MOFs are among the best values reported to date for MOF-based electrocatalysts,[12] and they outperform the OER performance of the commercially available RuO_2 catalyst (Figure 4d).

Furthermore, we conducted chronoamperometric studies at an overpotential of 255 mV to assess the long-term electrocatalytic stability of the Ni_2Fe_1 Sq-**zbr**-MOF OER catalyst. After 15 h of the chronoamperometric test, only a minor change in overpotential was observed and ≈92% of the OER activity was retained (Figure 4f). Moreover, we recorded the LSV scans of Ni_2Fe_1 Sq-**zbr**-MOF before and after long-term stability test (Figure S13, Supporting Information). Only a minor change in overpotential was observed even after 15 h of the chronoamperometric test (Figure 3a, Figure S13, Supporting Information). Importantly, PXRD analysis shows that Ni_2Fe_1 Sq-**zbr**-MOF and Ni_3Fe_1 Sq-**zbr**-MOF retain their crystallinity and structural integrity after long-term continuous oxygen evolution test (Figures S14–S16, Supporting Information). This shows that the high OER activity can be attributed to the seminal MOF structure. X-ray photoelectron spectroscopy (XPS) analysis of the Ni_2Fe_1 Sq-**zbr**-MOF electrodes before and after the chronoamperometric test not showed any change in oxidation state of metal ions (Figure S17, Supporting Information). Furthermore, we examined the electrochemical structural stability of other monometallic and bimetallic Sq-MOFs. Although monometallic and bimetallic Sq-MOF demonstrated high chemical stability in 1.0 M KOH electrolyte, their electrochemical structural stability varies depending on the metal ions from which they are developed. Under electrochemical OER conditions, Ni Sq-**zbr**-MOF shows high structural stability; the PXRD of the electrode after electrochemical OER shows the retention of the characteristic peaks of Sq-**zbr**-MOF phase (Figure S18, Supporting Information). However, the Co Sq-**zbr**-MOF shows low electrochemical structural stability (Figure S19, Supporting Information). To understand this difference in electrochemical stability of Sq-MOFs, we performed theoretical calculations for determining the formation energy and bond order. Theoretical calculations revealed that Ni Sq-**zbr**-MOF have a higher (absolute value) formation energy and higher bond order values in comparison to Co Sq-**zbr**-MOF, which could be the possible reason for the higher structural stability of Ni Sq-**zbr**-MOFs (Figure S20, Supporting Information). A bimetallic Sq-MOF with increased Ni^{2+} content, such as Co_1Ni_3, Ni_3Fe_1, Ni_2Fe_1, and Sq-**zbr**-MOFs, shows high electrochemical OER structural stability (Figures S12, S14, S15, Supporting Information). We observed that Fe_1Co_3 Sq-**zbr**-MOF showed low structural stability compared to Ni_3Fe_1 and Co_1Ni_3 Sq-MOFs, although they possess the same framework structure (Figure S21, Supporting Information). The **nbo-b** phase structure of Fe Sq-**nbo-b-**MOF and Fe-rich Fe-Ni Sq-**nbo-b**-MOFs are structurally labile to electrochemical OER operation conditions (Figure S19b, Supporting Information). Our studies show that increasing the relative ratio of Ni^{2+} in bimetallic Sq-**zbr**-MOF can significantly improve the overall electrochemical OER structural stability of the system.

2.3. Theoretical Calculations

To understand the low overpotential values and Tafel slope of the best bimetallic Ni_2Fe Sq-**zbr**-MOF compared to the pristine monometallic Ni Sq-**zbr**-MOF, density functional theory (DFT) calculations were performed to determine the Gibbs free energy of the various intermediate species involved in the electrochemical OER. Therefore, we considered linker-defective models in which the unsaturated metal sites are assumed for OER-active sites (**Figure 5**a). Such a strategy has previously been used successfully to model OER in MOFs and LDH materials.[18] For Ni_2Fe Sq-**zbr**-MOF, we considered two possible active sites, i.e., Ni- and Fe-labeled as Ni_2Fe-Ni-site Sq-**zbr**-MOF and Ni_2Fe-Fe-site Sq-**zbr**-MOF, respectively. The binding energies of OH^*, O^*, and OOH^* intermediate species involved in the OER process were calculated for these active sites. Figure 5b shows the Gibbs free energy of the formation for each elementary step of the OER computed for the four-electron reaction pathway. $OH^* \rightarrow O^* + (H^+ + e^-)$ was found to be the rate-determining step for all Sq-**zbr**-MOFs. The corresponding ΔG_{max}^{OER} is 2.42, 2.47, and 2.31 eV for Ni Sq-**zbr**-MOF, Ni_2Fe-Ni-site Sq-**zbr**-MOF, and Ni_2Fe-Fe-site Sq-**zbr**-MOF, respectively. Therefore, the calculated thermodynamic overpotential of the Ni_2Fe-Fe-site Sq-**zbr**-MOF (1.08 V) is significantly lower than the values obtained for Ni_2Fe-Ni-site (1.24 V), and Ni Sq-**zbr**-MOFs (1.19 V). These calculations confirm the experimental observations that Ni_2Fe Sq-**zbr**-MOF outperforms monometallic Ni Sq-**zbr**-MOF (Figure 4d) and reveal that the excellent performance of this catalyst can be attributed to the improved catalytic activity of the Fe site in Ni_2Fe Sq-**zbr**-MOF.

Note that additional analysis of the electronic structure evidenced that, compared to Ni Sq-**zbr**-MOF, Ni_2Fe Sq-**zbr**-MOF exhibits additional electronic states around the Fermi level (Figure 5c), in line with an improved electronic conductivity. This is experimentally confirmed by the low R_s value of Ni_2Fe Sq-**zbr**-MOF compared to Ni Sq-**zbr**-MOF obtained by electrochemical impedance spectroscopy (EIS) studies (Figure S22, Supporting Information). Analysis of the partial density of states (PDOS) reveals that the electronic states close to the Fermi level originate from Fe_{3d} and O_{2p} states. The *d*-band centers of Ni and Ni_2Fe-Fe-site Sq-**zbr**-MOFs were calculated to be −3.59 and −0.88 eV, respectively, indicating that the energy levels of the *d*-band center in the Ni_2Fe Sq-**zbr**-MOF structure are similar to the Fermi level. As per the *d*-band theory, the increased energy levels of the *d*-band center of Ni_2Fe Sq-**zbr**-MOF show that antibonding energy states increase. Thus, the interaction between the reactant and MOF is strengthened, which is beneficial for improving the adsorption capacity of intermediate species in the OER process.[19] Crystal orbital Hamilton population (COHP) analysis[20] was performed to identify bonding strength

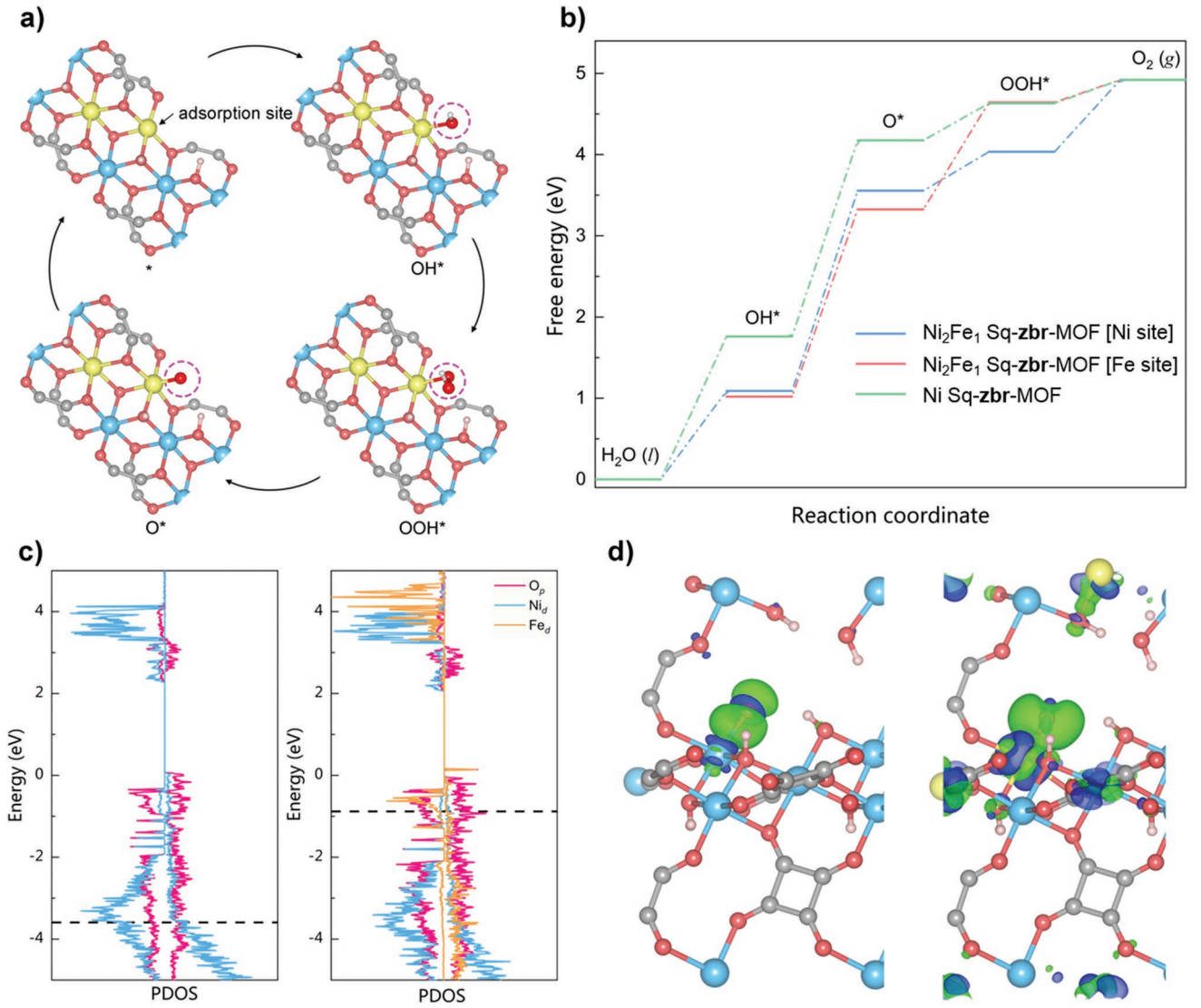

Figure 5. Theoretical studies on oxygen evolution reaction (OER) of Ni and Ni_2Fe Sq-zbr-MOFs. a) Schematic illustration of the proposed OER mechanism. The color code for the snapshots is the same as in Figure 1. For clarity, only metal nodes and adsorption intermediates are drawn in this figure. b) Standard free energy diagrams for OER at zero potential ($U = 0$) for Ni-, Ni_2Fe-Ni-site, and Ni_2Fe-Fe-site Sq-MOFs. c) Calculated projected density of states (PDOS) of Ni (left) Sq and Ni_2Fe-Fe-site (right) Sq-MOFs. The Fermi level was set as zero. The black dashed line represents the *d*-band center position of the active site. d) Calculated differential charge densities of O* adsorption on Ni- (left) and Ni_2Fe-Fe-site (right) Sq-zbr-MOFs, respectively. Charge accumulation and depletion are shown by green and blue, respectively (isosurface was set to 0.005 e $Å^{-2}$).

between the Fe-active site and O* intermediate (Figures S23 and S24, Supporting Information). Generally, the more positive the integrated COHP value, the weaker the binding strength. Therefore, in the Ni_2Fe-Fe-site Sq-**zbr**-MOF, the Fe site increases the binding strength between Fe and O* intermediate, resulting in a more favorable formation of O* and thus accelerates the OER process. Figure 5d shows the differential charge densities induced by the O adsorbed at the active site ($\Delta\rho = \rho_{*-O} - \rho_{*} - \rho_{O}$). As per the Bader charge analysis, additional electron transfer is observed in the Ni_2Fe-Fe-site Sq-**zbr**-MOF from the metal active site to O* in Ni Sq-MOF compared to the monometallic Ni Sq-**zbr**-MOF (Figure S25, Supporting Information).[21] Therefore, these DFT calculations demonstrate that charge transfer from the Sq-**zbr**-MOF to O* intermediate species enhances O* intermediate adsorption on the Ni_2Fe Sq-**zbr**-MOF, decreasing the thermodynamic overpotential for the OER process.

3. Conclusion

We developed a novel strategy for the synthesis of chemically robust Sq-**zbr**-MOFs for electrochemical OER reaction. Bimetallic Sq-**zbr**-MOFs with a **zbr** topology serve as an excellent platform for electrochemical OER owing to their open pore structure, presence of catalytically active 1D metal hydroxide strips, and high chemical resistance. We showed that regulation of the Ni^{2+} content in the bimetallic Sq-**zbr**-MOF system

is the key to achieve electrochemical structural stability toward OER. After testing various metal ratios, Ni_3Fe_1 and Ni_2Fe_1 Sq-**zbr**-MOFs were demonstrated to exhibit the optimal metal ratios for electrochemical OER in terms of catalytic activity and structural stability. Ni_2Fe_1 Sq-**zbr**-MOFs reveals a low overpotential of 230 mV (at 10 mA cm^{-2}) and a small Tafel slope of 37.7 mV dec^{-1}, with excellent long-term electrochemical stability for OER. Remarkably, Ni_2Fe_1 Sq-**zbr**-MOF outperforms commercially available noble-metal-based RuO_2 catalysts for the OER under identical operational conditions. Our studies demonstrate that chemically robust MOFs with metal hydroxide chains can be considered as a promising structural alternative to metal hydroxide/metal oxides in electrocatalysis.

4. Experimental Section

Synthesis of Monometallic and Bimetallic Squarate MOFs: Sq-MOFs based on metal (II) (metal (II) = Co^{2+}, Ni^{2+} or Fe^{2+}) were synthesized in a 100 mL Teflon-lined reactor under hydrothermal reaction conditions at 220 °C. For the pristine monometallic MOF synthesis, a mixture of 3,4-dihydroxy-3-cyclobutene-1,2-dione (squaric acid) (7.29 mmol, 1.5 eq.), metal (II) chloride hydrate (4.86 mmol, 1 eq.) (M = Co^{2+}, Fe^{2+} or Ni^{2+}), potassium hydroxide (19.4 mmol, 4 eq.), and water (17.5 mL) was transferred to a 100 mL Teflon-lined reactor. After 30 min of sonication, the Teflon-lined reactor was transferred to a preheated oven and heated to 220 °C for 72 h. After the reaction, the reactor was slowly cooled and Sq-MOF crystals were isolated using decantation and centrifugation. The Sq-MOF was repeatedly washed with D. I. water, exchanged with acetone and dried. Activation at 120 °C for 12 h was performed before gas adsorption measurements. For synthesizing bimetallic Sq-MOFs, the following ratios of mix metal ions were used M1: M2 = 1:3 (M1 = 1.215 mmol, M2 = 3.645 mmol), M1: M2 = 1:2 (M1 = 1.62 mmol, M2 = 3.24 mmol), M1: M2 = 1:1 (M1 = 2.43 mmol, M2 = 2.43 mmol), M1: M2 = 2:1 (M1 = 3.24 mmol, M2 = 1.62 mmol), and M_1: M_2 = 3:1 (M1 = 3.645 mmol, M2 = 1.215 mmol).

Preparation of Sq-MOF Electrodes: The working electrode was prepared as follows. To make a uniform electrocatalyst ink, 8 mg of grinded MOF electrocatalyst was mixed with 2 mg of nafion binder (in 1 mL of *N*-methyl-2-pyrrolidone (NMP) and ultrasonicated for 1 h. The electrocatalyst ink of 100 µL was uniformly casted on carbon paper with an active area of 1 cm^2, followed by drying at 100 °C under vacuum while maintaining an electrocatalyst loading of ≈0.8 mg cm^{-2}.

Electrochemical OER Measurements: Three electrode electrochemical setup (CHI Inc., 760E) with Hg-HgO as a reference electrode and a Pt wire as a counter electrode in 1.0 M KOH electrolyte was used for electrochemical analyses at room temperature. The working electrode was prepared with a carbon paper (1 × 3 cm) coated with an electrocatalyst (1 × 1 cm). All the electrode potential was then converted to reversible hydrogen electrode (RHE) scale using the following equation: $E_{(RHE)} = E_{(experimental)(Hg/HgO)} + 0.0591*pH + E_{0(Hg/HgO)}$ because $E_{0(Hg/HgO)}$ = 0.098 V versus NHE and 1.0 M KOH or pH = 14.

Therefore, $E_{(RHE)} = E_{(experimental)(Hg/HgO)} + 0.0591*pH + 0.098$ V.

iR correction (100%) was performed for all CVs and overpotentials using the EIS measured before the electrocatalysis. All CVs and LSVs were then recorded at a scan rate of 5 mV s^{-1}. Overpotential was determined by (η) = $E_{(RHE)}$ − 1.23 V, where $E_{(RHE)}$ was measured at a current density of 10 mA cm^{-2} (unless mentioned especially).

DFT Calculations: All DFT calculations were performed using the Vienna ab initio simulation package (Version: 5.4.4).[22] Projector augmented wave (PAW) pseudopotentials were obtained using the energy cutoff of 650 eV. The Perdew–Burke–Ernzerhof (PBE) generalized gradient approximations (GGA) were used to describe the exchange–correlation functional.[23] Grimme semiempirical DFT-D3 van der Waals force dispersion correction was used for all calculations.[24] Coulombic interactions were introduced using the GGA+*U* scheme to describe the strong correlation effects in Fe and Ni atoms. Hubbard *U* values for Fe and Ni atoms were obtained from previous studies (5.20 and 6.40 eV, respectively).[25] The structure models of Ni- and Ni_2Fe Sq-MOF (1×1×2) supercells with a *k*-mesh of 3 × 3 × 2 grid in reciprocal space were used to identify the OER activity sites. An implicit solvation method, as implemented in the VASPsol package, was used to consider solvation effect in the reaction.[26] Bader charge analysis was used to decompose the charge density.[21] Chemical bonding analysis was performed using the LOBSTER package.[20b] Moreover, additional details of the calculations, i.e., entropy, zero-point energy corrections, and COHP have been reported in the Supporting Information section.

Supporting Information

Supporting Information is available from the Wiley Online Library or from the author.

Acknowledgements

This work was financially supported by King Abdullah University of Science and Technology (KAUST). The computational work has received funding from KAUST under Center Partnership Fund Program (CPF 2910), and was granted access to the HPC resources of CINES under the allocation A0120907613 made by GENCI.

Conflict of Interest

The authors declare no conflict of interest.

Data Availability Statement

The data that support the findings of this study are available from the corresponding author upon reasonable request.

Keywords

bimetallic, electrocatalysis, metal–organic frameworks, oxygen evolution reaction, redox chemistry

Received: August 30, 2022
Revised: October 11, 2022
Published online: November 18, 2022

[1] Z. W. Seh, J. Kibsgaard, C. F. Dickens, I. Chorkendorff, J. K. Norskov, T. F. Jaramillo, *Science* **2017**, *355*, eaad4998.
[2] a) M. Hoel, S. Kvemdokk, *Resour. Energy Econ.* **1996**, *18*, 115; b) I. Dincer, C. Acar, *Int. J. Energy Res.* **2015**, *39*, 585; c) S. Chu, A. Majumdar, *Nature* **2012**, *488*, 294; d) N. S. Lewis, D. G. Nocera, *Proc. Natl. Acad. Sci. U. S. A.* **2006**, *103*, 15729.
[3] a) A. Midilli, I. Dincer, *Int. J. Hydrogen Energy* **2008**, *33*, 4209; b) J. A. Turner, *Science* **2004**, *305*, 972; c) J. O. M. Bockris, *Int. J. Hydrogen Energy* **2008**, *33*, 2129.
[4] a) K. Scott, *Electrochemical Methods for Hydrogen Production*, The Royal Society of Chemistry, London **2020**, Ch. 1; b) H. B. Gray, *Nat. Chem.* **2009**, *1*, 7; c) X. Zou, Y. Zhang, *Chem. Soc. Rev.* **2015**, *44*, 5148; d) Y. Shi, B. Zhang, *Chem. Soc. Rev.* **2016**, *45*, 1529.
[5] a) Y. Jiao, Y. Zheng, M. Jaroniec, S. Z. Qiao, *Chem. Soc. Rev.* **2015**, *44*, 2060; b) M. S. Fabera, S. Jin, *Energy Environ. Sci.* **2014**, *7*, 3519.

[6] a) S. Anantharaj, V. Aravindan, *Adv. Energy Mater.* **2020**, *10*, 1902666; b) K. S. Joya, Y. F. Joya, K. Ocakoglu, R. Van De Krol, *Angew. Chem., Int. Ed.* **2013**, *52*, 10426; c) J. Song, C. Wei, Z.-F. Huang, C. Liu, L. Zeng, X. Wang, Z. J. Xu, *Chem. Soc. Rev.* **2020**, *49*, 2196; d) N.-T. Suen, S.-F. Hung, Q. Quan, N. Zhang, Y.-J. Xu, H. M. Chen, *Chem. Soc. Rev.* **2017**, *46*, 337; e) V. S. Kale, U. Sim, J. Yang, K. Jin, S.-I. Chae, W. J. Chang, A. K. Sinha, H. Ha, C.-C. Hwang, J. An, H.-K. Hong, Z. Lee, K. T. Nam, T. Hyeon, *Small* **2017**, *13*, 1603893.

[7] a) R. Kötz, S. Stucki, *Electrochim. Acta* **1986**, *31*, 1311; b) J. Yu, Q. He, G. Yang, W. Zhou, Z. Shao, M. Ni, *ACS Catal.* **2019**, *9*, 9973; c) S.-Y. Bae, J. Mahmood, I.-Y. Jeon, J.-B. Baek, *Nanoscale Horiz.* **2020**, *5*, 43.

[8] a) B. Zhang, X. Zheng, O. Voznyy, R. Comin, M. Bajdich, M. Garcia-Melchor, L. Han, J. Xu, M. Liu, L. Zheng, F. P. Garcia de Arquer, C. T. Dinh, F. Fan, M. Yuan, E. Yassitepe, N. Chen, T. Regier, P. Liu, Y. Li, P. De Luna, A. Janmohamed, H. L. Xin, H. Yang, A. Vojvodic, E. H. Sargent, *Science* **2016**, *352*, 333; b) L. Han, S. Dong, E. Wang, *Adv. Mater.* **2016**, *28*, 9266; c) I. Roger, M. A. Shipman, M. D. Symes, *Nat. Rev. Chem.* **2017**, *1*, 0003.

[9] a) F. Dionigi, P. Strasser, *Adv. Energy Mater.* **2016**, *6*, 1600621; b) M. Gong, Y. Li, H. Wang, Y. Liang, J. Z. Wu, J. Zhou, J. Wang, T. Regier, F. Wei, H. Dai, *J. Am. Chem. Soc.* **2013**, *135*, 8452; c) J. Zhao, J. J. Zhang, Z. Y. Li, X. H. Bu, *Small* **2020**, *16*, 2003916; d) S. Lee, K. Banjac, M. Lingenfelder, X. Hu, *Angew. Chem., Int. Ed.* **2019**, *58*, 10295.

[10] a) J. Y. C. Chen, L. N. Dang, H. F. Liang, W. L. Bi, J. B. Gerken, S. Jin, E. E. Alp, S. S. Stahl, *J. Am. Chem. Soc.* **2015**, *137*, 15090; b) F. Song, X. Hu, *Nat. Commun.* **2014**, *5*, 4477.

[11] a) H. Li, M. Eddaoudi, M. O'Keeffe, O. M. Yaghi, *Nature* **1999**, *402*, 276; b) M. Eddaoudi, J. Kim, N. Rosi, D. Vodak, J. Wachter, M. O'Keeffe, O. M. Yaghi, *Science* **2002**, *295*, 469; c) H. Jiang, D. Alezi, M. Eddaoudi, *Nat. Rev. Mater.* **2021**, *6*, 466; d) C. J. Doonan, C. J. Sumby, *CrystEngComm* **2017**, *19*, 4044; e) J. Gascon, A. Corma, F. Kapteijn, F. X. Llabrés i Xamena, *ACS Catal.* **2014**, *4*, 361; f) L. Jiao, Y. Wang, H. L. Jiang, Q. Xu, *Adv. Mater.* **2018**, *30*, 1703663; g) S. Li, Y. Gao, N. Li, L. Ge, X. Bu, P. Feng, *Energy Environ. Sci.* **2021**, *14*, 1897; h) W. Zhou, D. D. Huang, Y. P. Wu, J. Zhao, T. Wu, J. Zhang, D. S. Li, C. H. Sun, P. Y. Feng, X. H. Bu, *Angew. Chem., Int. Ed.* **2019**, *58*, 4227.

[12] a) S. Zhao, C. Tan, C.-T. He, P. An, F. Xie, S. Jiang, Y. Zhu, K.-H. Wu, B. Zhang, H. Li, J. Zhang, Y. Chen, S. Liu, J. Dong, Z. Tang, *Nat. Energy* **2020**, *5*, 881; b) S. Zhao, Y. Wang, J. Dong, C.-T. He, H. Yin, P. An, K. Zhao, X. Zhang, C. Gao, L. Zhang, J. Lv, J. Wang, J. Zhang, A. M. Khattak, N. A. Khan, Z. Wei, J. Zhang, S. Liu, H. Zhao, Z. Tang, *Nat. Energy* **2016**, *1*, 16184. c) L. Sun, C. H. Hendon, M. A. Minier, A. Walsh, M. Dincă, *J. Am. Chem. Soc.* **2015**, *137*, 6164.

[13] a) Q. Qian, Y. Li, Y. Liu, L. Yu, G. Zhang, *Adv. Mater.* **2019**, *31*, 1901139; b) H.-F. Wang, L. Chen, H. Pang, S. Kaskel, Q. Xu, *Chem. Soc. Rev.* **2020**, *49*, 1414; c) X. Wang, L. Yu, B. Y. Guan, S. Song, X. W. Lou, *Adv. Mater.* **2018**, *30*, 1801211.

[14] a) S. O. H. Gutschke, M. Molinier, A. K. Powell, P. T. Wood, *Angew. Chem.* **1997**, *109*, 1028; b) S. Sharma, M. Jansen, *Z. Anorg. Allg. Chem.* **2008**, *634*, 1911.

[15] a) S. Goswami, A. Adhikary, H. S. Jena, S. Biswas, S. Konar, *Inorg. Chem.* **2013**, *52*, 12064; b) J. Greve, C. Nather, *Acta Crystallogr.* **2002**, *E58*, m653.

[16] a) L. Y. Li, L. D. Guo, Z. G. Zhang, Q. W. Yang, Y. W. Yang, Z. B. Bao, Q. L. Ren, J. Li, *J. Am. Chem. Soc.* **2019**, *141*, 9358; b) T. He, X. Kong, Z. Bian, Y. Zhang, G. Si, L. Xie, X. Wu, H. Huang, Z. Chang, X. Bu, M. Zaworotko, Z. Nie, J. Li, *Nat. Mater.* **2022**, *21*, 689; c) T. He, X. J. Kong, J. Zhou, C. Zhao, K. Wang, X. Q. Wu, X. L. Lv, G. R. Si, J. R. Li, Z. R. Nie, *J. Am. Chem. Soc.* **2021**, *143*, 9901; d) X.-L. Lv, K. Wang, B. Wang, J. Su, X. Zou, Y. Xie, J.-R. Li, H.-C. Zhou, *J. Am. Chem. Soc.* **2017**, *139*, 211.

[17] Z. Cai, X. Bu, P. Wang, J. C. Ho, J. Yang, X. Wang, *J. Mater. Chem. A* **2019**, *7*, 5069.

[18] a) P. Liao, J. A. Keith, E. A. Carter, *J. Am. Chem. Soc.* **2012**, *134*, 13296; b) Z. Xue, K. Liu, Q. Liu, Y. Li, M. Li, C.-Y. Su, N. Ogiwara, H. Kobayashi, H. Kitagawa, M. Liu, G. Li, *Nat. Commun.* **2019**, *10*, 5048.

[19] a) H. Lee, O. Gwon, K. Choi, L. Zhang, J. Zhou, J. Park, J.-W. Yoo, J.-Q. Wang, J. H. Lee, G. Kim, *ACS Catal.* **2020**, *10*, 4664; b) S. Sun, X. Zhou, B. Cong, W. Hong, G. Chen, *ACS Catal.* **2020**, *10*, 9086.

[20] a) R. Dronskowski, P. E. Blöchl, *J. Phys. Chem.* **1993**, *97*, 8617; b) R. Nelson, C. Ertural, J. George, V. L. Deringer, G. Hautier, R. Dronskowski, *J. Comput. Chem.* **2020**, *41*, 1931.

[21] W. Tang, E. Sanville, G. Henkelman, *J. Phys.: Condens. Matter* **2009**, *21*, 084204.

[22] G. Kresse, J. Furthmüller, *Phys. Rev. B* **1996**, *54*, 11169.

[23] J. P. Perdew, K. Burke, M. Ernzerhof, *Phys. Rev. Lett.* **1996**, *77*, 3865.

[24] S. Grimme, *J. Comput. Chem.* **2006**, *27*, 1787.

[25] a) A. Jain, S. P. Ong, G. Hautier, W. Chen, W. D. Richards, S. Dacek, S. Cholia, D. Gunter, D. Skinner, G. Ceder, K. A. Persson, *APL Mater.* **2013**, *1*, 011002; b) L. Wang, T. Maxisch, G. Ceder, *Phys. Rev. B* **2006**, *73*, 195107.

[26] K. Mathew, R. Sundararaman, K. Letchworth-Weaver, T. A. Arias, R. G. Hennig, *J. Chem. Phys.* **2014**, *140*, 084106.